Mid- and High-frequency Resonance Characteristics and Suppression Strategies of VSC-UHVDC for Large-scale Renewable Energy Transmission

Junjie Feng, Wang Xiang, Jinyu Wen, Chuang Fu, Qingming Xin, Xiaobin Zhao, Changyue Zou, Biyue Huang, and Zhiyong Yuan

***Abstract*—Mid- and high-frequency resonance (MHFR) is highly likely to occur at the sending end of voltage source converter-based ultra-high voltage direct current (VSC-UHVDC) for large-scale renewable energy transmission. It is of great importance to investigate the resonance characteristics and the corresponding suppression strategies. Firstly, this paper introduces the overall control scheme of VSC-UHVDC for large-scale renewable energy transmission. Then, the impedance models of VSC under grid-forming control with AC voltage coordinated control are established. The mid- and high-frequency impedance characteristics of VSC-UHVDC are analyzed. The key factors affecting the impedance characteristics have been revealed, including the AC voltage control, the voltage feedforward, the inner current loop, the positive-sequence and negative-sequence independent control (PSNSIC), and the control delay. The MHFR characteristics at the sending-end system are analyzed in the whole operation process, including the black start and the normal power transmission operation. An integrated control scheme is proposed to address the MHFR problems. Finally, extensive case studies are conducted on a planned VSC-UHVDC project to verify the theoretical analysis.**

***Index Terms*—Large-scale renewable energy, voltage source converter-based ultra-high voltage direct current (UHVDC), mid- and high-frequency resonance, suppression measure.**

I. Introduction

THE development and utilization of large-scale renewable energy serve as an effective means to reduce carbon emissions [1]. Voltage source converter-based ultra-high voltage direct current (VSC-UHVDC) emerges as an important means for large-scale renewable energy transmission, owing to its advantages such as flexible control and voltage support for island systems [2], [3]. VSC-UHVDC scheme will be adopted in several large-scale renewable energy transmission projects in China, such as those from Southeast Tibet to Guangdong, and Gansu to Zhejiang. However, with high penetration of power electronics, the sending-end grid is relatively weak, resulting in potential oscillation risks between the sending-end grid and VSC-UHVDC [4]-[6]. It has been reported that the resonance problem occurs in two pilot voltage source converter-based high-voltage direct current (VSC-HVDC) projects in China, namely, the 59 Hz, 750 Hz, 1550 Hz, and 4000 Hz oscillations in the Zhangbei DC grid project [1], [7], and the 320 Hz, 2000 Hz, and 2500 Hz oscillations in Rudong offshore wind farm HVDC transmission project [8], [9].

Compared with VSC-HVDC/UHVDC connected to traditional AC grid or VSC-HVDC connected to renewable energy, VSC-UHVDC system for large-scale renewable energy transmission scenarios exhibits two new characteristics. ① Since multiple converters are connected in parallel on the AC side in ultra-high voltage (UHV) systems, grid-forming control with AC voltage coordinated control should be adopted [10] - [12]. The newly introduced coordinated control, along with its new control delay feature, will significantly impact the impedance characteristics, which have rarely been studied in previous research works. ② During black start operation mode of the VSC-UHVDC connected to large-scale renewable energy, the sending-end grid exhibits multiple resonance points with capacitance effects across a wide frequency range, which increases the risk of mid- and high-frequency resonance (MHFR) [7]. Therefore, it is essential to analyze the MHFR characteristics of the system and propose effective suppression strategies.

The interaction between the inductive negative damping of VSC-UHVDC and the capacitive weak damping of the AC grid is the main reason for MHFR [13]-[20]. At present, mainly three kinds of methods are proposed to address MHFR, which are control delay reduction, control system optimi-

Manuscript received: March 20, 2024; revised: May 7, 2024; accepted: May 22, 2024. Date of CrossCheck: May 22, 2024. Date of online publication: June 25, 2024.

This work was supported by National Key Research and Development Program of China (No. 2023YFB2405900) and the Technology Project of China Southern Power Grid (No. ZBKJXM20232198).

J. Feng, W. Xiang, and J. Wen (corresponding author) are with the School of Electrical and Electronic Engineering, Huazhong University of Science and Technology, Wuhan, China, and J. Feng is also with Electric Power Research Institute, China Southern Power Grid Co., Ltd., Guangzhou, China (e-mail: fengjj@csg.cn; xiangwang1003@hust.edu.cn; jinyu.wen@hust.edu.cn).

C. Fu, Q. Xin, X. Zhao, C. Zou, B. Huang, and Z. Yuan are with Electric Power Research Institute, China Southern Power Grid Co., Ltd., Guangzhou, China (e-mail: fuchuang@csg.cn; xinqm@csg.cn; zhaoxb@csg.cn; zoucy@csg.cn; yuanzy1@csg.cn; huangby3@csg.cn).

DOI: 10.35833/MPCE.2024.000301

zation, and passive damping [14]-[17], [21]-[26]. Reducing control delay can significantly decrease the risk of MHFR. But control delay is unavoidable, resulting in inherent negative damping characteristics in the converter [16]. The situation is even worse in VSC-UHVDC with AC voltage coordinated control due to a longer and more complex delay feature. The optimization of the control system primarily focuses on modifying the control structure and parameters. Adding low-pass filters, such as second-order low-pass filters [14], nonlinear filters [15], in the voltage feedforward is one of the most widely used methods. Whereas filter-based methods are not suitable for VSC-UHVDC with grid-forming control, as the interaction between the AC control loop and voltage feedforward is neglected. Additionally, reducing the parameters of proportional integral (PI) controller in the current loop is an effective measure to mitigate MHFR [16], but the design of PI parameters is too experience-relied. Besides, the active damping and adaptive control can also suppress MHFR [22]-[24]. However, it can only provide effective suppression within a limited frequency range and is not suitable for AC grid with multiple resonance points. To mitigate the problem, weak feedback control strategy has been proposed for Zhangbei and Rudong projects, which lacks transient current regulation capabilities [7]. Regarding passive damping, parallel or series passive filters can be utilized to reshape the impedance of converter [25], [26], at the expense of increased footprint and cost of the converter station.

In summary, the existing suppression strategies encounter challenges in addressing the emerging MHFR issues in the VSC-UHVDC for large-scale renewable energy transmission, owing to the new characteristics introduced by AC voltage coordinated control, new control delay feature, and the sending-end grid. Currently, there is a lack of thorough discussion regarding how the aforementioned factors influence the MHFR characteristics, and an efficient control scheme is also necessary to be proposed. This paper studies the MHFR characteristics of VSC-UHVDC for large-scale renewable energy transmission, and then proposes an integrated control scheme to cope with the MHFR problems in the whole operation process, including the black start and the normal power transmission operation of the system. The main contributions can be summarized as follows:

1) This paper first analyzes the MHFR characteristics of VSC-UHVDC for the new scenario. The analysis results reveal that AC voltage control associated with its new control delay feature has a significant influence on the MHFR characteristics. Besides, the high risk of MHFR during black start operations under closed-loop control is also observed.

2) An integrated control scheme, which consists of a novel impedance reshaping measure and a smooth open-loop and closed-loop adaptive control strategy, is proposed to address the MHFR problem during normal operation and black start operation, respectively.

The remainder of this paper is organized as follows. Section II describes the structure of the large-scale renewable energy transmission by VSC-UHVDC. Section III presents the modeling of VSC-UHVDC impedance at the sending end. Section IV analyzes the impedance characteristics of the VSC-UHVDC. Section V proposes the impedance reshaping measures. Section VI evaluates the risk of MHFR between the sending-end grid and the VSC-UHVDC. Section VII proposes smooth open-loop and closed-loop adaptive control. Section VII concludes this paper.

II. Structure of Large-scale Renewable Energy Transmission by VSC-UHVDC

A. Overall Scheme

The overall technical scheme of VSC-UHVDC for large-scale renewable energy transmission is shown in Fig. 1. At the sending end, the renewable energy base consists of four 220 kV/500 kV photovoltaic (PV) step-up substations, each with a capacity of about 4000 MW, connected with six or seven 35 kV/220 kV PV step-up substations. PV plant 1 is connected to PV plant 2 through AC line 1. Subsequently, PV plant 2 is connected to PV plant 3 through AC line 2. PV plant 3 is connected to PV plant 4 through AC line 3, and then PV plant 4 is connected to the sending-end converter station of the VSC-UHVDC through AC line 4 with a length of about 300 km. The sending-end capacity of the VSC-UHVDC is 10000 MW, which is achieved by jointly constructing two 5000 MW units, S1 and S2, in the same station. The power is transmitted to the receiving-end stations, S3 and S4, located in the load center, through the ±800 kV DC line, which has a length of about 2500 km.

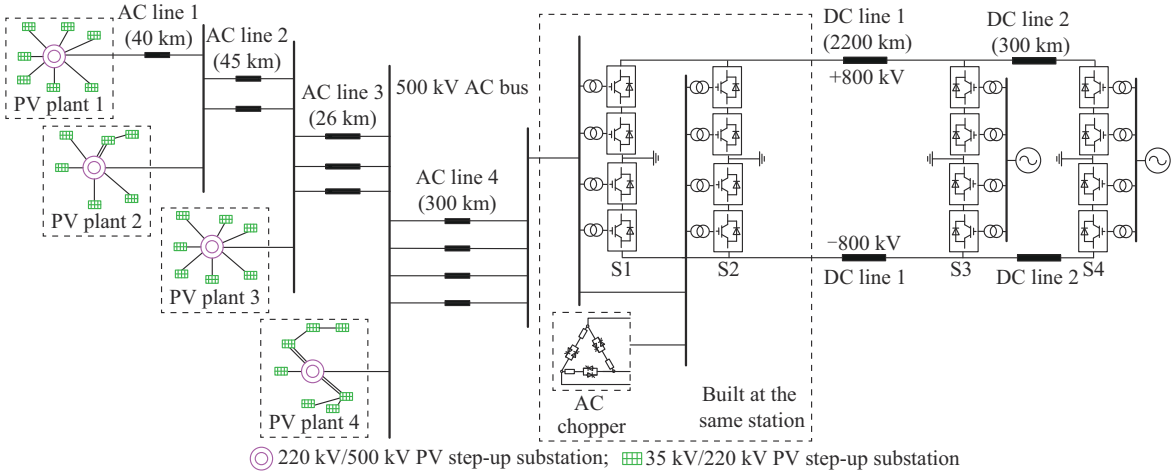

Fig. 1. Overall technical scheme of VSC-UHVDC for large-scale renewable energy transmission.

B. Control System

The sending-end converters of VSC-UHVDC need to implement grid-forming control to offer voltage support for renewable energy sources. As shown in Fig. 2, the voltage-current double-loop control with positive-sequence and negative-sequence independent control (PSNSIC) is adopted. The VSC-UHVDC station comprises 4 converters connected in parallel on the AC side and in series on the DC side. Hence, AC voltage coordinated control is required. The AC voltage control loop shared by bipolar four converters is set at the station control layer to generate the current reference of the station. Distribution coefficients K_1-K_4 are set at the pole control layer to generate the reference for bipolar four converters, so as to distribute their transmission power. In Fig. 2, u and i are the voltage and current, respectively; subscripts d and q represent the d-axis and q-axis components, respectively; subscripts A, B, and C represent the three phases; subscripts P and N represent the positive-sequence and negative-sequence components, respectively; superscripts ref and * represent the reference value and modulation wave, respectively; ω_1 is the fundamental angular frequency; K_d is the current decoupling coefficient; and G_{fv} and G_{fc} are the low-pass filters.

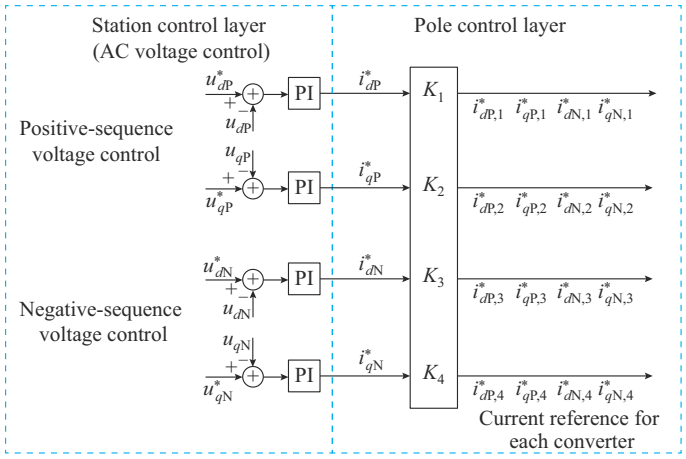

(a)

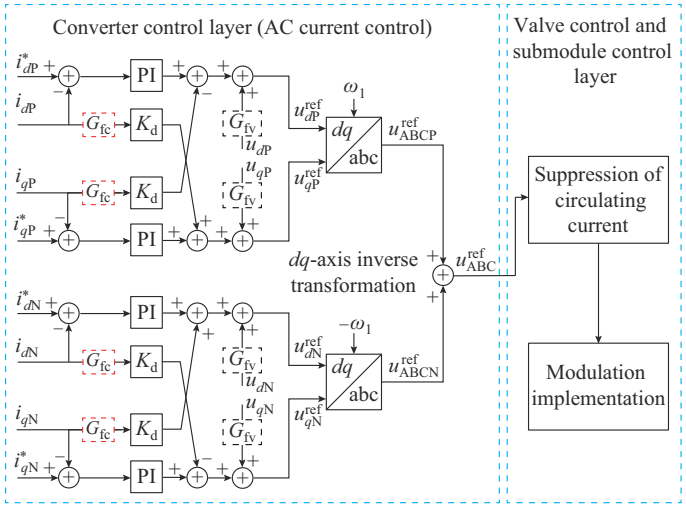

(b)

Fig. 2. Control structure of VSC at sending end. (a) AC voltage control. (b) AC current control.

The control link of the grid-forming VSC-UHVDC requires an additional station layer and pole layer compared with VSC-HVDC or the grid-following VSC-UHVDC, resulting in increased control delay. Moreover, there will be different control delays for the outer and inner loops, which will impact the MHFR characteristics. The inner current loop is recognized as a crucial factor that contributes to the MHFR in VSC-UHVDC [14] - [16]. Therefore, this paper will explore the possibility of eliminating the inner current loop by adopting voltage single-loop control or open-loop control. In the case of voltage single-loop control, only the AC voltage control loop, shown in Fig. 2(a), is maintained and it generates the modulation wave for each converter.

III. Modeling of VSC-UHVDC Impedance at Sending End

A. Modeling of Converter Impedance

When analyzing the MHFR problem, it is reasonable to neglect the influence of frequency coupling and internal circulating currents of the converter [14], [16]. However, the influence of PSNSIC should be taken into consideration. The harmonic linearization method is used to model the VSC-UHVDC impedance according to the following steps.

1) Step 1: Calculation of Voltage and Current in Frequency Domain

The converter with AC voltage control does not require a phase-locked loop, and the angle for abc/dq-axis transformation is directly set as $\theta_1 = \omega_1 t$. The frequency domain expressions of positive-sequence dq-axis voltage are derived as:

$$u_{dP}(f) = \begin{cases} G_{sv}(\mathrm{j}2\pi f_1)V_1 & \text{DC component} \\ G_{sv}(s \pm \mathrm{j}2\pi f_1)G_{sd}V_P & f = \pm(f_P - f_1) \\ G_{sv}(s \mp \mathrm{j}2\pi f_1)G_{sd}V_N & f = \pm(f_N + f_1) \end{cases} \tag{1}$$

$$u_{qP}(f) = \begin{cases} \mp\mathrm{j}G_{sv}(s \pm \mathrm{j}2\pi f_1)G_{sd}V_P & f = \pm(f_P - f_1) \\ \pm\mathrm{j}G_{sv}(s \mp \mathrm{j}2\pi f_1)G_{sd}V_N & f = \pm(f_N + f_1) \end{cases} \tag{2}$$

where V_1 corresponds to the magnitude of the fundamental voltage at frequency f_1; V_P corresponds to the magnitude of the positive-sequence voltage perturbation at frequency f_P; V_N corresponds to the magnitude of the negative-sequence voltage perturbation at frequency f_N; G_{sv} is the transfer function of voltage sampling; G_{sd} is the transfer function of the delay filter with 1/4 fundamental frequency period, and $G_{sd} = 0.5(1 + \mathrm{e}^{-sT/4})$; and T is the fundamental frequency period. Similarly, the positive-sequence dq-axis currents in the frequency domain are derived as:

$$i_{dP}(f) = \begin{cases} G_{si}(\mathrm{j}2\pi f_1)I_1\cos(\varphi_1) & \text{DC component} \\ G_{si}(s \pm \mathrm{j}2\pi f_1)G_{sd}I_P & f = \pm(f_P - f_1) \\ G_{si}(s \mp \mathrm{j}2\pi f_1)G_{sd}I_N & f = \pm(f_N + f_1) \end{cases} \tag{3}$$

$$i_{qP}(f) = \begin{cases} G_{si}(\mathrm{j}2\pi f_1)I_1\sin(\varphi_1) & \text{DC component} \\ \mp\mathrm{j}G_{si}(s \pm \mathrm{j}2\pi f_1)G_{sd}I_P & f = \pm(f_P - f_1) \\ \pm\mathrm{j}G_{si}(s \mp \mathrm{j}2\pi f_1)G_{sd}I_N & f = \pm(f_N + f_1) \end{cases} \tag{4}$$

where I_1 and φ_1 corresponds to the magnitude and phase of the fundamental current, respectively; I_P and I_N represent the positive-sequence and negative-sequence perturbations of current, respectively; and G_{si} is the transfer function of the current sampling.

In the negative-sequence abc/*dq*-axis transformation, the reference angle is $-\omega_1 t$. Similarly, the negative-sequence *dq*-axis voltage and current in the frequency domain are obtained as:

$$u_{dN}(f)=\begin{cases}G_{sv}(s\mp j2\pi f_1)G_{sd}V_P & f=\pm(f_P+f_1)\\ G_{sv}(s\pm j2\pi f_1)G_{sd}V_N & f=\pm(f_N-f_1)\end{cases} \tag{5}$$

$$u_{qN}(f)=\begin{cases}\mp jG_{sv}(s\mp j2\pi f_1)G_{sd}V_P & f=\pm(f_P+f_1)\\ \pm jG_{sv}(s\pm j2\pi f_1)G_{sd}V_N & f=\pm(f_N-f_1)\end{cases} \tag{6}$$

$$i_{dN}(f)=\begin{cases}G_{si}(s\mp j2\pi f_1)G_{sd}I_P & f=\pm(f_P+f_1)\\ G_{si}(s\pm j2\pi f_1)G_{sd}I_N & f=\pm(f_N-f_1)\end{cases} \tag{7}$$

$$i_{qN}(f)=\begin{cases}\mp jG_{si}(s\mp j2\pi f_1)G_{sd}I_P & f=\pm(f_P+f_1)\\ \pm jG_{si}(s\pm j2\pi f_1)G_{sd}I_N & f=\pm(f_N-f_1)\end{cases} \tag{8}$$

2) Step 2: Calculation of dq-axis Modulation Waves

After *Step 1*, the positive-sequence and negative-sequence *dq*-axis modulation voltages $u_{dP}^{ref}(f)$, $u_{qP}^{ref}(f)$, $u_{dN}^{ref}(f)$, and $u_{qN}^{ref}(f)$ can be calculated based on the control structure shown in Fig. 2. The calculation should take into account the control delays. The control system receives input variables such as AC voltage, AC current, and voltage feedforward. These three control variables traverse different control channels, as illustrated in Fig. 3, resulting in varying control delays for each variable. The control delay transfer functions of AC voltage, AC current, and voltage feedforward under voltage-current double-loop control can be defined as G_{dv}, G_{di}, and G_{df}, respectively.

$$G_{dx}=e^{-sT_{dx}}\frac{1-e^{-sT_s}}{sT_s}\quad x=v,i,f \tag{9}$$

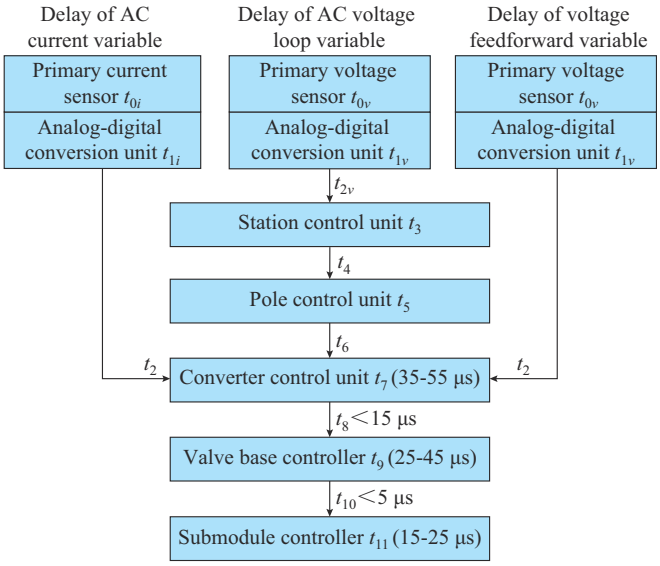

Fig. 3. Components of control delay.

where T_{dx} is the control delay of each variable; and T_s is the control cycle.

With voltage single-loop control, the modulation wave is obtained at the station control layer, and it will be directly sent to the valve control layer, indicating that the component of control delay excludes pole control and converter control layers.

3) Step 3: Calculation of abc-axis Modulation Wave

According to the time domain expression of *dq*/abc-axis transformation, the positive-sequence and negative-sequence modulation waves of phase A in the frequency domain can be derived by convolution calculation of *dq*-axis modulation wave and transformation coefficient, as shown in (10).

$$\begin{cases}u_{AP}^{ref}(f)=F[\cos\theta_1]*u_{dP}^{ref}(f)+F[-\sin\theta_1]*u_{qP}^{ref}(f)\\ u_{AN}^{ref}(f)=F[\cos\theta_1]*u_{dN}^{ref}(f)+F[\sin\theta_1]*u_{qN}^{ref}(f)\end{cases} \tag{10}$$

where $F[x]$ is the Fourier solution; and * represents the convolution calculation. Thus, the modulation wave in the frequency domain $u_A^{ref}(f)$ is derived as:

$$u_A^{ref}(f)=u_{AP}^{ref}(f)+u_{AN}^{ref}(f) \tag{11}$$

4) Calculation of Impedance

The control delay and discrete control have been considered in the calculation of *dq*-axis modulation wave. Therefore, the modulation wave can be deemed equivalent to its output voltage $u_A^{out}(f)$. According to Kirchhoff's Law, the relation between the output voltage and grid-side voltage of the converter is:

$$u_A^{out}(f)-u_A(f)=sLi_A(f) \tag{12}$$

where $u_A(f)$ is the AC grid voltage; $i_A(f)$ is the AC current; and L is the equivalent inductance of the converter. Assuming that $u_A(f)$ includes V_P and V_N, and $i_A(f)$ includes I_P and I_N, $u_A^{out}(f)$ will also include V_P, V_N, I_P, and I_N. When $f=f_P$, the ratio of positive-sequence voltage disturbance to current disturbance V_P/I_P is the positive-sequence impedance of converter. When $f=f_N$, the ratio of negative-sequence voltage disturbance to current disturbance V_N/I_N is the negative-sequence impedance.

B. Voltage Single-loop Control

If the VSC-UHVDC system adopts voltage single-loop control, the *dq*-axis modulation waves in frequency domain are derived as:

$$u_{dP}^{ref}(f)=\begin{cases}u_{dP0}^{ref} & \text{DC component}\\ -G_{sd}G_{AC}G_{sv}G_{dvs}V_P & f=\pm(f_P-f_1)\\ -G_{sd}G_{AC}G_{sv}G_{dvs}V_N & f=\pm(f_N+f_1)\end{cases} \tag{13}$$

$$u_{qN}^{ref}(f)=\begin{cases}u_{qP0}^{ref} & \text{DC component}\\ \pm jG_{sd}G_{AC}G_{sv}G_{dvs}V_P & f=\pm(f_P-f_1)\\ \mp jG_{sd}G_{AC}G_{sv}G_{dvs}V_N & f=\pm(f_N+f_1)\end{cases} \tag{14}$$

where G_{dvs} is the control delay transfer function of AC voltage under single-loop control.

According to (10), the positive-sequence modulation wave of phase A can be obtained as:

$$u_{\mathrm{AP}}^{\mathrm{ref}}(f)=\begin{cases}\dfrac{1}{2}u_{d\mathrm{P0}}^{\mathrm{ref}}\pm\dfrac{\mathrm{j}}{2}u_{q\mathrm{P0}}^{\mathrm{ref}} & f=\pm f_1\\ -G_{\mathrm{sd}}^{+}G_{\mathrm{AC}}^{+}G_{\mathrm{sv}}G_{\mathrm{dv}}V_{\mathrm{P}} & f=\pm f_{\mathrm{P}}\\ -G_{\mathrm{sd}}^{-}G_{\mathrm{AC}}^{-}G_{\mathrm{sv}}G_{\mathrm{dv}}V_{\mathrm{N}} & f=\pm f_{\mathrm{N}}\end{cases}\tag{15}$$

Similarly, the negative-sequence modulation wave of phase A can be obtained as:

$$u_{\mathrm{AN}}^{\mathrm{ref}}(f)=\begin{cases}-G_{\mathrm{sd}}^{-}G_{\mathrm{AC}}^{-}G_{\mathrm{sv}}G_{\mathrm{dv}}V_{\mathrm{P}} & f=\pm f_{\mathrm{P}}\\ -G_{\mathrm{sd}}^{+}G_{\mathrm{AC}}^{+}G_{\mathrm{sv}}G_{\mathrm{dv}}V_{\mathrm{N}} & f=\pm f_{\mathrm{N}}\end{cases}\tag{16}$$

where $u_{d\mathrm{P0}}^{\mathrm{ref}}$ and $u_{q\mathrm{P0}}^{\mathrm{ref}}$ correspond to the magnitudes of the fundamental voltage modulation wave; G_{AC} is the transfer function of PI controller in the outer AC voltage loop; and the superscripts + and – in the transfer function represent different frequency offsets, where $G^{+}=G(s-\mathrm{j}\omega_1)$ and $G^{-}=G(s+\mathrm{j}\omega_1)$. Thus, according to (11) and (12), the positive-sequence and negative-sequence impedances of the converter with voltage single-loop control are obtained as:

$$Z_{\mathrm{P}}=\frac{sL}{1+\left(G_{\mathrm{sd}}^{+}G_{\mathrm{AC}}^{+}+G_{\mathrm{sd}}^{-}G_{\mathrm{AC}}^{-}\right)G_{\mathrm{sv}}G_{\mathrm{dv}}}\tag{17}$$

$$Z_{\mathrm{N}}=\frac{sL}{1+\left(G_{\mathrm{sd}}^{-}G_{\mathrm{AC}}^{-}+G_{\mathrm{sd}}^{+}G_{\mathrm{AC}}^{+}\right)G_{\mathrm{sv}}G_{\mathrm{dv}}}\tag{18}$$

C. Voltage-current Double-loop Control

If the VSC-UHVDC adopts voltage-current double-loop control, the positive-sequence and negative-sequence modulation waves in frequency domain are derived as:

$$u_{\mathrm{AP}}^{\mathrm{ref}}(f)=\begin{cases}\dfrac{1}{2}u_{d\mathrm{P0}}^{\mathrm{ref}}\pm\dfrac{\mathrm{j}}{2}u_{q\mathrm{P0}}^{\mathrm{ref}} & f=\pm f_1\\ -G_{\mathrm{sv}}G_{\mathrm{dv}}G_{\mathrm{sd}}^{+}G_{\mathrm{AC}}^{+}G_{\mathrm{i}}^{+}K_xV_{\mathrm{P}}+G_{\mathrm{sv}}G_{\mathrm{df}}G_{\mathrm{sd}}^{+}V_{\mathrm{P}}-\\ \qquad\left(G_{\mathrm{i}}^{+}\mp\mathrm{j}K_{\mathrm{d}}\right)G_{\mathrm{si}}G_{\mathrm{di}}G_{\mathrm{sd}}^{+}I_{\mathrm{P}} & f=\pm f_{\mathrm{P}}\\ -G_{\mathrm{sv}}G_{\mathrm{dv}}G_{\mathrm{sd}}^{-}G_{\mathrm{AC}}^{-}G_{\mathrm{i}}^{-}K_xV_{\mathrm{N}}+G_{\mathrm{sv}}G_{\mathrm{df}}G_{\mathrm{sd}}^{-}V_{\mathrm{N}}-\\ \qquad\left(G_{\mathrm{i}}^{-}\pm\mathrm{j}K_{\mathrm{d}}\right)G_{\mathrm{si}}G_{\mathrm{di}}G_{\mathrm{sd}}^{-}I_{\mathrm{N}} & f=\pm f_{\mathrm{N}}\end{cases}\tag{19}$$

$$u_{\mathrm{AN}}^{\mathrm{ref}}(f)=\begin{cases}-G_{\mathrm{sv}}G_{\mathrm{dv}}G_{\mathrm{sd}}^{-}G_{\mathrm{AC}}^{-}G_{\mathrm{i}}^{-}K_xV_{\mathrm{P}}+G_{\mathrm{sv}}G_{\mathrm{df}}G_{\mathrm{sd}}^{-}V_{\mathrm{P}}-\\ \qquad\left(G_{\mathrm{i}}^{-}\pm\mathrm{j}K_{\mathrm{d}}\right)G_{\mathrm{si}}G_{\mathrm{sd}}^{-}I_{\mathrm{P}} & f=\pm f_{\mathrm{P}}\\ -G_{\mathrm{sv}}G_{\mathrm{dv}}G_{\mathrm{sd}}^{+}G_{\mathrm{AC}}^{+}G_{\mathrm{i}}^{+}K_xV_{\mathrm{N}}+G_{\mathrm{sv}}G_{\mathrm{df}}G_{\mathrm{sd}}^{+}V_{\mathrm{N}}-\\ \qquad\left(G_{\mathrm{i}}^{+}\mp\mathrm{j}K_{\mathrm{d}}\right)G_{\mathrm{si}}G_{\mathrm{di}}G_{\mathrm{sd}}^{+}I_{\mathrm{N}} & f=\pm f_{\mathrm{N}}\end{cases}\tag{20}$$

where G_{i} is the transfer function of the PI controller in inner current loop. In (19) and (20), the modulation waves consist of three polynomials, representing the impact of outer AC voltage loop, voltage feedforward, and current control, respectively. The positive-sequence and negative-sequence impedances of converter with voltage-current double-loop control are obtained as:

$$Z_{\mathrm{P}}=\frac{sL+\left(G_{\mathrm{i}}^{+}G_{\mathrm{sd}}^{+}-\mathrm{j}K_{\mathrm{d}}G_{\mathrm{sd}}^{+}+G_{\mathrm{i}}^{-}G_{\mathrm{sd}}^{-}+\mathrm{j}K_{\mathrm{d}}G_{\mathrm{sd}}^{-}\right)G_{\mathrm{si}}G_{\mathrm{di}}}{1-G_{\mathrm{df}}G_{\mathrm{sv}}+G_{\mathrm{sv}}G_{\mathrm{dv}}K_x\left(G_{\mathrm{sd}}^{+}G_{\mathrm{AC}}^{+}G_{\mathrm{i}}^{+}+G_{\mathrm{i}}^{-}G_{\mathrm{sd}}^{-}G_{\mathrm{AC}}^{-}\right)}\tag{21}$$

$$Z_{\mathrm{N}}=\frac{sL+\left(G_{\mathrm{i}}^{-}G_{\mathrm{sd}}^{-}+\mathrm{j}K_{\mathrm{d}}G_{\mathrm{sd}}^{-}+G_{\mathrm{i}}^{+}G_{\mathrm{sd}}^{+}-\mathrm{j}K_{\mathrm{d}}G_{\mathrm{sd}}^{+}\right)G_{\mathrm{si}}G_{\mathrm{di}}}{1-G_{\mathrm{df}}G_{\mathrm{sv}}+G_{\mathrm{sv}}G_{\mathrm{dv}}K_x\left(G_{\mathrm{sd}}^{-}G_{\mathrm{AC}}^{-}G_{\mathrm{i}}^{-}+G_{\mathrm{sd}}^{+}G_{\mathrm{AC}}^{+}G_{\mathrm{i}}^{+}\right)}\tag{22}$$

IV. Analysis of Impedance Characteristics of VSC-UHVDC

This section analyzes the impedance characteristics of VSC-UHVDC with voltage single-loop control and voltage-current double-loop control, respectively. The parameters of converter are listed in Table I. If no filter is conducted during sampling, transfer functions G_{sv} and G_{si} are equivalent to 1, as the delays of voltage sampling and current sampling are included in total control delays G_{dv}, G_{di}, and G_{df}.

TABLE I
Parameters of Converter

Category	Parameter	Value
Rated power	Rated active power (MW)	1250
	Rated reactive power (Mvar)	±250
Transformer	Connection group	Yny
	Transformation ratio (kV/kV)	525/244
	Capacity (MVA)	467×3
	Short-circuit impedance	18%
Valve	Rated operation voltage of module (V)	2100
	Capacitance of module (mF)	18
	Number of submodules per bridge arm	205
	Voltage on DC side (kV)	400
	Arm inductor (mH)	40
Control system	Proportional and integral coefficients of current loop PI controller	1, 10
	Proportional and integral coefficients of voltage loop PI controller	1 (or 0.5), 100
	Current distribution coefficient K_x	1
	AC voltage channel delay T_{dv} (μs)	250
	Voltage feedforward channel delay T_{di} (μs)	200
	Current channel delay T_{df} (μs)	200
	Voltage single-loop control delay T_{dvs} (μs)	200
	Modulation cycle T_{s} (μs)	100

A. Voltage Single-loop Control

1) Impedance Characteristic of Voltage Single-loop Control

The impedance characteristic of the converter with voltage single-loop control is shown in Fig. 4. There is a high-frequency resonance peak in the impedance magnitude accompanied by significant high-frequency negative damping.

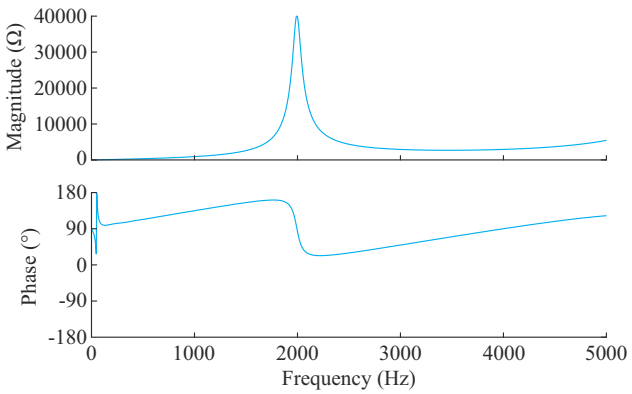

Fig. 4. Impedance characteristic of converter with voltage single-loop control.

Since the zero-order holder can be approximately equivalent to half of the control cycle delay, the disturbance term introduced by voltage feedback can be written as:

$$G_{\mathrm{dv}}G_{\mathrm{sv}} \approx \mathrm{e}^{-\mathrm{j}2\pi f T_{\mathrm{delay}}} \tag{23}$$

where the total system delay $T_{\mathrm{delay}} = T_{\mathrm{dvs}} + T_s/2$. Since the integral term of PI controller in mid- and high-frequency range can be approximately equivalent to 0, and $G_{\mathrm{sd}}^{+} + G_{\mathrm{sd}}^{-} = 1$, the impedance of the converter can be simplified as:

$$Z_{\mathrm{P/N}} = \frac{sL}{1 + K_{\mathrm{pac}}\mathrm{e}^{-\mathrm{j}2\pi f T_{\mathrm{delay}}}} \tag{24}$$

where K_{pac} is the proportional coefficient, and $K_{\mathrm{pac}}\mathrm{e}^{-\mathrm{j}2\pi f T_{\mathrm{delay}}}$ changes periodically within the range of -1 to 1. When $f \approx (2k-1)/(2T_{\mathrm{delay}})$, where k is a non-zero positive integer, the denominator term $1 + K_{\mathrm{pac}}\mathrm{e}^{-\mathrm{j}2\pi f T_{\mathrm{delay}}} \approx 0$, leading to the appearance of resonance points in the high-frequency range. Additionally, (24) indicates that the main factors impacting the converter impedance are K_{pac} of the PI controller, the control delay, and the equivalent inductance on the AC side.

2) Improvement Effect of Impedance Characteristics Based on Voltage Low-pass Filter

To improve the impedance characteristics, a low-pass filter can be added to the voltage loop and the proportional coefficient of the PI controller can be reduced. A second-order low-pass filter with a cutoff frequency of 100 Hz is added to the voltage loop, and the impedance characteristics of the converter under different proportional coefficients are shown in Fig. 5.

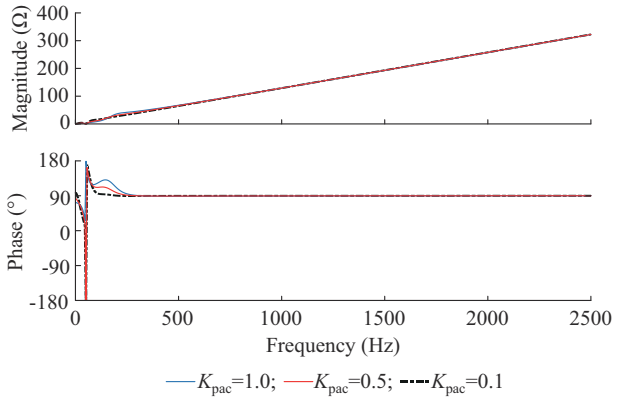

Fig. 5. Impedance frequency characteristic of converter under different proportional coefficients.

After adopting the low-pass filter, the negative damping of the converter impedance at high-frequency range is effectively suppressed. A smaller proportional coefficient of the PI controller results in a better effect on impedance reshaping. However, the converter still exhibits negative damping in the mid-frequency range of 100-300 Hz, leading to a high risk of resonance in this frequency range. Additionally, if the converter only adopts the voltage single-loop control, it is unable to regulate the bridge arm current, resulting in a risk of transient overcurrent. Therefore, a transient current switching control mode must be designed to prevent overcurrent under fault conditions. Moreover, the dynamic performance of the converter will be further reduced after adding the low-pass filter. Given a comprehensive consideration of resonance suppression and dynamic performance, it is advisable not to substitute voltage-current double-loop control with voltage single-loop control for resonance suppression.

B. Voltage-current Double-loop Control

Since $\mathrm{j}G_{\mathrm{sd}}^{-} - \mathrm{j}G_{\mathrm{sd}}^{+} = \mathrm{e}^{-sT/4}$, the impedance of the converter with double-loop control can be simplified as:

$$Z_{\mathrm{P/N}} \approx \frac{sL + \left(K_{\mathrm{p,i}} \pm K_{\mathrm{d}}\mathrm{e}^{-sT/4}\right)\mathrm{e}^{-\mathrm{j}2\pi f T_{\mathrm{delayi}}}}{1 - \mathrm{e}^{-\mathrm{j}2\pi f T_{\mathrm{delayf}}} + K_x K_{\mathrm{p,AC}} K_{\mathrm{p,i}}\mathrm{e}^{-\mathrm{j}2\pi f T_{\mathrm{delayv}}}} \tag{25}$$

where sL and $\left(K_{\mathrm{p,i}} \pm K_{\mathrm{d}}\mathrm{e}^{-sT/4}\right)\mathrm{e}^{-\mathrm{j}2\pi f T_{\mathrm{delayi}}}$ represent the disturbances of equivalent inductance and AC current control, respectively; $\mathrm{e}^{-\mathrm{j}2\pi f T_{\mathrm{delayf}}}$ and $K_x K_{\mathrm{p,AC}} K_{\mathrm{p,i}}\mathrm{e}^{-\mathrm{j}2\pi f T_{\mathrm{delayv}}}$ represent the disturbances of voltage feedforward and outer AC voltage loop, respectively; $T_{\mathrm{delayi}} = T_{\mathrm{di}} + T_s/2$; $T_{\mathrm{delayv}} = T_{\mathrm{dv}} + T_s/2$; $T_{\mathrm{delayf}} = T_{\mathrm{df}} + T_s/2$; and $K_{\mathrm{p,AC}}$ and $K_{\mathrm{p,i}}$ are the proportional coefficients of PI controller in outer AC voltage loop and inner current loop, respectively.

Compared with traditional grid-following control, the grid-forming control introduces an outer AC voltage loop disturbance which is determined by current distribution coefficient, the proportional coefficient of the PI controller in outer AC voltage loop and inner current loop, and control delay of AC voltage control channel.

Due to the influence of voltage feedforward, a resonance peak in high-frequency range exists in the impedance magnitude of the converter with grid-following control accompanied by significant negative damping, as shown by the red dotted line in Fig. 6. A low-pass filter is typically added to the voltage feedforward to improve impedance characteristics of converter with grid-following control. If a low-pass filter is also added to the voltage feedforward of the converter with grid-forming control, the impedance is simplified as (26), and the impedance characteristics are shown by the blue solid line in Fig. 6.

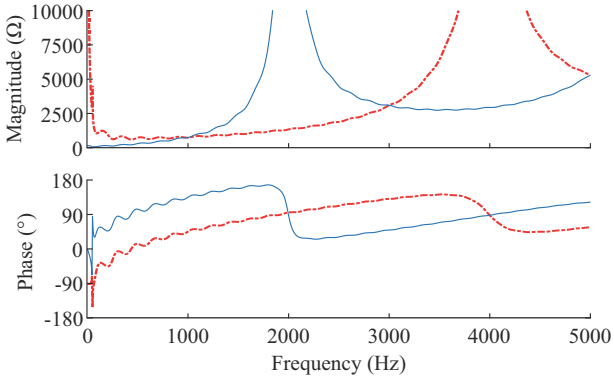

Fig. 6. Influence of voltage feedforward on impedance characteristics of converter with double-loop control.

$$Z_{\mathrm{P/N}} \approx \frac{sL + \left(K_{\mathrm{p,i}} \pm K_{\mathrm{d}}\mathrm{e}^{-sT/4}\right)\mathrm{e}^{-\mathrm{j}2\pi f T_{\mathrm{delayi}}}}{1 + K_x K_{\mathrm{p,AC}} K_{\mathrm{p,i}}\mathrm{e}^{-\mathrm{j}2\pi f T_{\mathrm{delayv}}}} \tag{26}$$

It can be observed that the negative damping of the converter with grid-forming control is not suppressed. On the

contrary, compared with the red dotted line, the frequency of the first resonance point is advanced to 2000 Hz, and the corresponding negative damping frequency range shifts to 400-2000 Hz, leading to a significant deterioration in the impedance characteristics. The main reason is that, although the low-pass filter can compensate for the disturbance caused by voltage feedforward, there is still a disturbance term $K_x K_{\mathrm{p,AC}} K_{\mathrm{p,i}} \mathrm{e}^{-\mathrm{j}2\pi f T_{\mathrm{delayv}}}$ introduced by AC voltage control in the denominator of the converter impedance. When $K_x K_{\mathrm{p,AC}} K_{\mathrm{p,i}} \mathrm{e}^{-\mathrm{j}2\pi f T_{\mathrm{delayv}}} = -1$, the denominator of the impedance becomes 0, resulting in the generation of a resonance peak in the impedance magnitude.

To sum up, the MHFR suppression measures by adding low-pass filter to voltage feedforward cannot be directly applied to grid-forming converters.

V. Impedance Reshaping Measures

A. Voltage Coordinated Optimization Control

According to (25), the disturbance term $-\mathrm{e}^{-\mathrm{j}2\pi f T_{\mathrm{delayf}}}$ introduced by voltage feedforward is in the same form as the disturbance term $K_x K_{\mathrm{p,AC}} K_{\mathrm{p,i}} \mathrm{e}^{-\mathrm{j}2\pi f T_{\mathrm{delayv}}}$ introduced by AC voltage control, but with different coefficients. If (27) is satisfied, the disturbance terms can be eliminated.

$$\begin{cases} K_x K_{\mathrm{p,AC}} K_{\mathrm{p,i}} = 1 \\ T_{\mathrm{delayf}} = T_{\mathrm{delayv}} \end{cases} \tag{27}$$

Since the control system operates in per-unit value, $K_x K_{\mathrm{p,AC}} K_{\mathrm{p,i}} = 1$ can be easily achieved by parameter setting in practice, for example, K_x, $K_{\mathrm{p,AC}}$, and $K_{\mathrm{p,i}}$ can all be set to 1. The outer AC voltage loop and voltage feedforward can utilize the same control variable to ensure that T_{delayf} is equal to T_{delayv}. This involves the station control layer, sending the AC voltage sampling value along with the current reference to the pole control layer. Then, the pole control layer forwards this AC voltage sampling value to the converter control layer as the voltage feedforward control variable.

Figure 7 shows that, after adopting the voltage coordinated optimization control, the converter impedance is greatly improved. The resonance peak of impedance magnitude disappears, and the phase of the mid- and high-frequency impedance is around 90°. If either of the two conditions in (27) cannot be met, the impedance reshaping effect will be poor.

It should be noted that by adding low-pass filters both to voltage feedforward and outer AC voltage loop, the disturbance term in the denominator of the impedance can also be eliminated. Both nonlinear filter and low-pass filter can be used for voltage feedforward. However, the nonlinear filter or a low-pass filter with an excessively low cutoff frequency is not suitable for outer AC voltage control, leading to limitations in improving impedance characteristics. This is attributed to AC voltage itself being a controlled variable. Besides, adding low-pass filters to voltage feedforward and outer AC voltage loop will sacrifice the dynamic performance of the system. The comparison analysis of dynamic performance with different impedance reshaping measure is presented in the Appendix A.

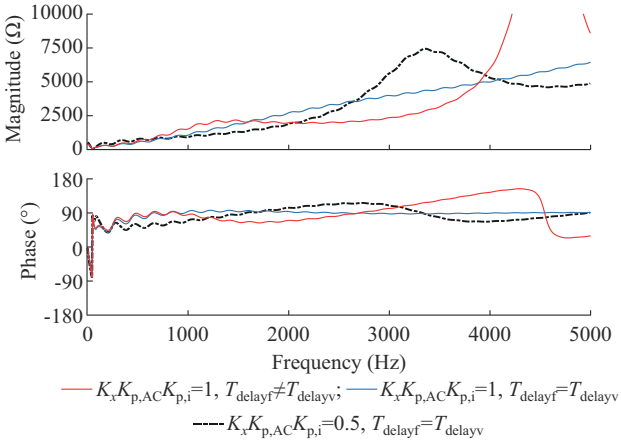

Fig. 7. Impedance characteristics of VSC with voltage coordinated optimization control.

B. Optimization of Inner Current Loop

Once the disturbances caused by voltage feedforward and outer AC voltage control are eliminated, the impedance of the converter can be simplified as:

$$Z_{\mathrm{p/N}} \approx sL + \left(K_{\mathrm{p,i}} \pm K_{\mathrm{d}} \mathrm{e}^{-sT/4}\right) \mathrm{e}^{-\mathrm{j}2\pi f T_{\mathrm{delayi}}} \tag{28}$$

Obviously, there remains a disturbance term resulting from the interaction between inner current loop and control delay. This results in negative damping of the converter impedance in the mid- and high-frequency ranges. The disturbance term primarily depends on three factors: ① the control delay in the current channel; ② the proportional coefficient of the PI controller in the inner current loop; ③ the PSNSIC, as the PSNSIC introduces a delay filter with 1/4 fundamental frequency period that interacts with decoupling control, resulting in fluctuations with a period of 200 Hz in the impedance characteristic curve.

To reshape the impedance characteristics of VSC, the inner current loop control can be optimized in three ways as follows.

1) Reduce the control delay: the control delay can be reduced by implementing direct transmission of pure optical measurement signals, improving the performance of control devices, employing full-link gigabit communication for critical paths among multiple devices, and optimizing the key control links.

2) Reduce the proportional coefficient of the PI controller in current loop: since reducing the proportional coefficient will impact the dynamic performance of the system, the proportional coefficient should be carefully designed based on the evaluation of the dynamic performance of the system. The evaluation method for proportional coefficient is illustrated in Fig. 8. The minimum proportional coefficient can be determined by assessing whether the bridge arm current of the converter with different coefficients meets the requirements during a three-phase short-circuit fault in the AC grid.

3) Current decoupling optimization control: it can be achieved by two strategies. The first is to add a low-pass filter in *dq*-axis current decoupling control, as shown in Fig. 2. The second way is to use a constant current as the control input for *dq*-axis current decoupling control. This constant cur-

rent can be obtained by dividing the steady-state power after average value filtering by the steady-state voltage. After optimization control, the disturbance caused by interaction between the decoupling control and PSNSIC can be eliminated, thereby reducing the maximum impedance phase of the converter.

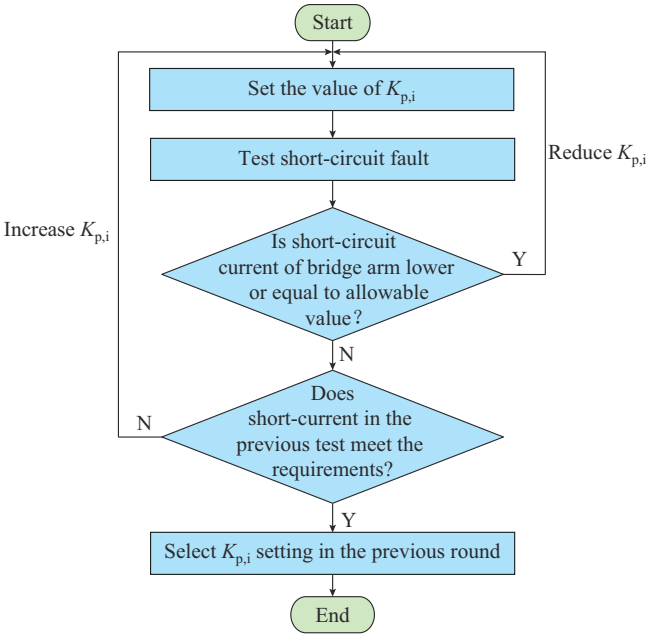

Fig. 8. Evaluation method for proportional coefficient.

After implementing the above impedance reshaping measures, the converter impedance is obtained, as shown in Fig. 9. Before optimizing the inner current loop control, the maximum phase of the converter impedance in the mid- and high-frequency range is 95.67°. The maximum impedance phase in the mid- and high-frequency range is decreased to 93.54° by reducing the proportional coefficient of the inner current loop PI controller from 1.0 to 0.5. Furthermore, the maximum impedance phase in the mid- and high-frequency range is further reduced to 91.89° by implementing current decoupling optimization control.

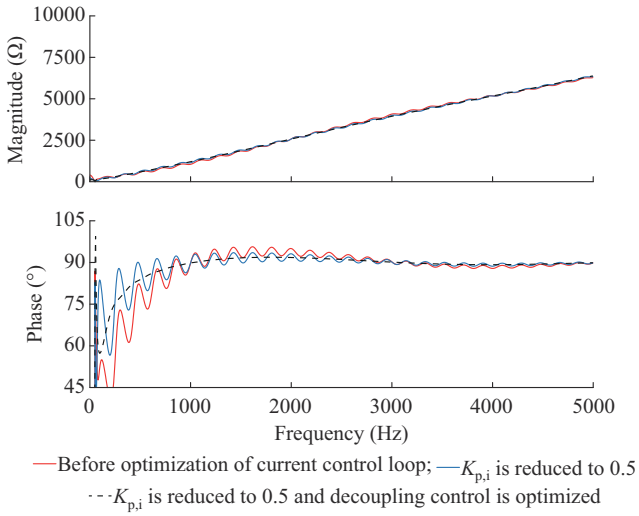

Fig. 9. Impedance characteristics of VSC after optimizing current control.

VI. Resonance Risk Evaluation Between Renewable Energy Base and VSC-UHVDC

Since there exists significant difference in the impedance characteristics of the renewable energy base during the black start and the normal power transmission operation, this section analyzes the MHFR characteristics for the two operations, respectively.

A. Power Transmission of Renewable Energy Base

The renewable energy station is connected to the VSC-UHVDC through multi-stage step-up substation. The impedance of the renewable energy base is affected by factors such as the grid-connected inverter, collection structure, AC line, and reactive power compensation. As this paper focuses on the characteristics of VSC-UHVDC system, the impedance of the renewable energy base is obtained by impedance scanning, as shown in Fig. 10. Although PV inverters exhibit negative damping in their impedance, the impedance of sending-end grid still demonstrates positive damping. This is because the negative damping is counteracted by the equivalent resistance of transformers and transmission lines.

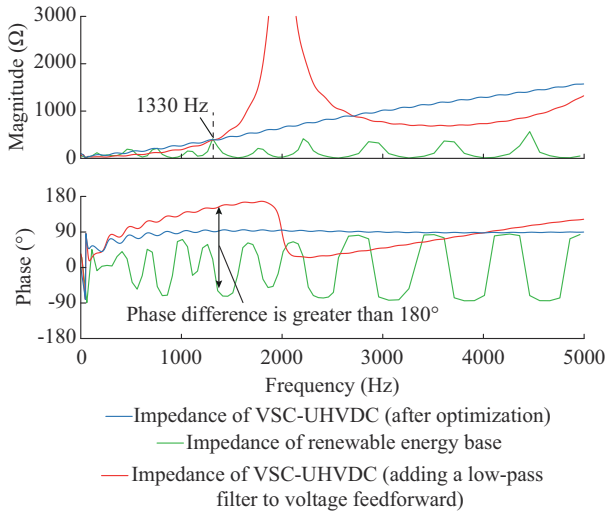

Fig. 10. Comparison of impedance characteristics between VSC-UHVDC and renewable energy base.

If the sending-end converter of VSC-UHVDC adopts the same MHFR suppression strategy as the traditional grid-following converter, which involves adding a low-pass filter to the voltage feedforward, a comparison of the impedance characteristics between the VSC-UHVDC and the renewable energy base is shown in Fig. 10.

There is an intersection of impedance magnitude between the VSC-UHVDC and the renewable energy base at 1330 Hz, and the phase difference is greater than 180° at the cut-off frequency, indicating a high-frequency resonance risk in the system. To reshape the impedance of the VSC-UHVDC, voltage coordinated optimization control is adopted. This ensures that the phase difference between the VSC-UHVDC and the renewable energy base is less than 180° within a wide-band range, effectively suppressing the MHFR in the system.

A simulation on resonance characteristic analysis is conducted in PSCAD/EMTDC. In the simulation, the 35 kV/220 kV PV step-up substations are equivalently aggregated, considering the impedance characteristics of the PV inverter and feeder lines within the station. The transmission line adopts the Bergeron model to simulate the high-frequency impedance characteristics accurately. Figure 11 shows the voltage and current waveforms at the point of common coupling (PCC) before and after impedance reshaping of the VSC-UHVDC station. After the system is started and enters a steady state, the VSC-UHVDC converter is switched to the traditional MHFR suppression measure by adding a low-pass filter to the voltage feedforward at 3.8 s. The system resonates at 1325 Hz. At 4 s, the impedance reshaping measure is put into operation. The high-frequency resonance gradually attenuates and is effectively suppressed. To sum up, the correctness of the theoretical analysis is verified.

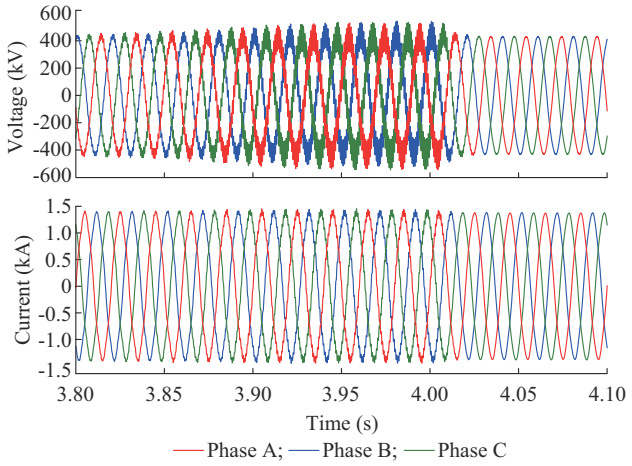

Fig. 11. Voltage and current waveforms at PCC before and after impedance reshaping of VSC-UHVDC station.

B. Black Start of Renewable Energy Base

During the black start of renewable energy base, the operation modes of VSC-UHVDC with no-load AC bus or no-load AC line are involved, both of which pose a high risk of MHFR. When the converter operates with a no-load AC bus, the impedance of the AC system is determined by the stray capacitance of the AC bus and converter transformer, which are purely capacitive. If the converter station operates with no-load AC line, the impedance of the AC system is mainly determined by the frequency characteristic of AC line. This subsection focuses on the analysis during VSC-UHVDC with no-load AC line. The AC lines can be equivalently transformed into π-type circuits, as illustrated in Fig. 12.

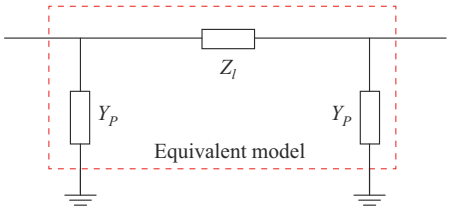

Fig. 12. Equivalent model of AC line.

In Fig. 12, the expressions of Z_l and Y_P are given as:

$$\begin{cases} Z_l = Z_c \sinh(\gamma l) \\ Y_P = \dfrac{\cosh(\gamma l) - 1}{Z_c \sinh(\gamma l)} \end{cases} \tag{29}$$

where l is the length of the AC line; Z_c is the wave impedance of the AC line; γ is the propagation constant of the AC line; and $\sinh(\gamma l)$ and $\cosh(\gamma l)$ are the hyperbolic sine function and hyperbolic cosine function, respectively.

$$\gamma = R_0 / 2\sqrt{C_0 / L_0} + \mathrm{j}\omega_1 \sqrt{L_0 C_0} \tag{30}$$

$$Z_c = \sqrt{L_0 / C_0} - \mathrm{j}R_0 / \left(2\omega_1 \sqrt{L_0 C_0}\right) \tag{31}$$

where R_0, L_0, and C_0 are the resistance, inductance, and capacitance per unit length, respectively.

In Fig. 1, AC line 4 is 300 km and is equipped with 50% series compensation. The impedance of no-load AC line is shown in Fig. 13. The impedance magnitude of the transmission line contains multiple high-frequency resonance points, and the phase varies between ±90°, which can easily match the VSC-UHVDC impedance, thus exciting MHFR. The comparison of impedance characteristics between the VSC-UHVDC and the renewable energy base during the black start operation with no-load AC lines is shown in Fig. 13.

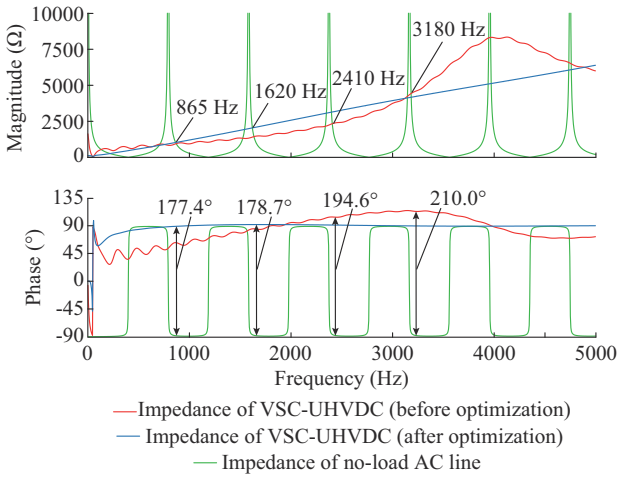

Fig. 13. Comparison of impedance characteristics between VSC-UHVDC and renewable energy base during black start.

Before optimizing the impedance of converter (with $K_{\mathrm{p,AC}}$ as 0.5, K_x and K_{pi} as 1), there are multiple intersection points of impedance magnitude between VSC-UHVDC and renewable energy base. The corresponding phase differences at 3180 Hz and 2410 Hz are 210.0° and 194.6°, respectively, indicating that the system is at a high-frequency resonance risk. The MHFR suppression strategy proposed in Section V is adopted to reshape the converter impedance. There are still multiple intersection points of impedance magnitude between VSC-UHVDC and the renewable energy base, among which the corresponding phase differences at 865 Hz and 1620 Hz are 177.4° and 178.7°, respectively. Although MHFR can be suppressed, the system stability margin remains low.

The analysis of resonance characteristics is verified in PSCAD/EMTDC. The VSC-UHVDC utilizes the control structure shown in Fig. 2. During startup, the AC voltage reference is ramped up from 0 to 1.0 p.u. with a ramping slope of 4.0 p.u./s. As shown in Fig. 14, before the impedance reshaping measures are adopted, VSC-UHVDC exhibits divergent high-frequency resonance. The resonant frequencies primarily occur at 3150 Hz and 2400 Hz, aligning with the theoretical analysis. Moreover, there are some harmonics at 1600 Hz and 850 Hz. This is because there is an intersection point between the impedance magnitude of VSC-UHVDC and renewable energy base at this frequency, but the corresponding phase difference does not exceed 180°, and the VSC-UHVDC shows weak damping in this mode.

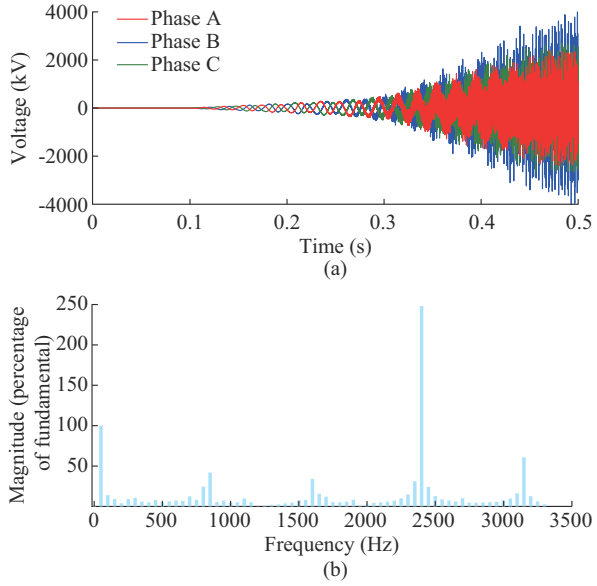

Fig. 14. AC voltage waveform and spectrum analysis results before impedance reshaping of VSC-UHVDC. (a) AC voltage waveform at PCC. (b) Spectrum analysis at PCC.

After the impedance reshaping measure is adopted, the AC voltage waveform at PCC is shown in Fig. 15.

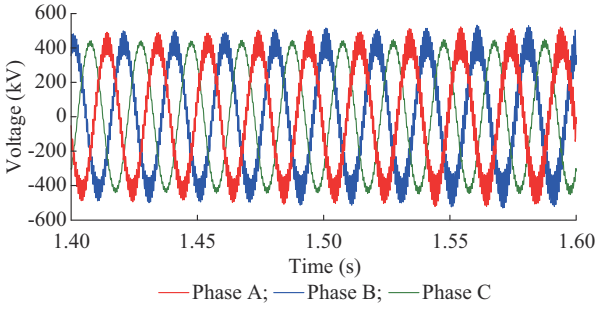

Fig. 15. AC voltage waveforms at PCC.

The sending-end system is able to successfully complete a black start. However, there are still significant number of 1620 Hz harmonics during steady state. The main reason is that although the MHFR is suppressed, the system stability margin remains low. The above simulation results are consistent with the theoretical analysis results, thereby validating the theoretical analysis.

VII. Smooth Open-loop and Closed-loop Adaptive Control

The negative damping in the mid- and high-frequency range of VSC-UHVDC cannot be completely eliminated through closed-loop controller optimization, and there is still a resonance risk at the sending-end grid, especially during black start operation. Therefore, open-loop and closed-loop adaptive control can be adopted, as shown in Fig. 16. The open-loop control mode is adopted during black start operation. If the active power exceeds a certain threshold or the system failure occurs, the closed-loop control mode is switched to ensure the steady-state operation and fault ride-through performance. In Fig. 16, P_c^* is the power threshold; F_o is the closed-loop control enabling mark bit; U_p^* is the fault detection reference voltage; and θ_0 is the initial reference phase of the dq-axis transformation.

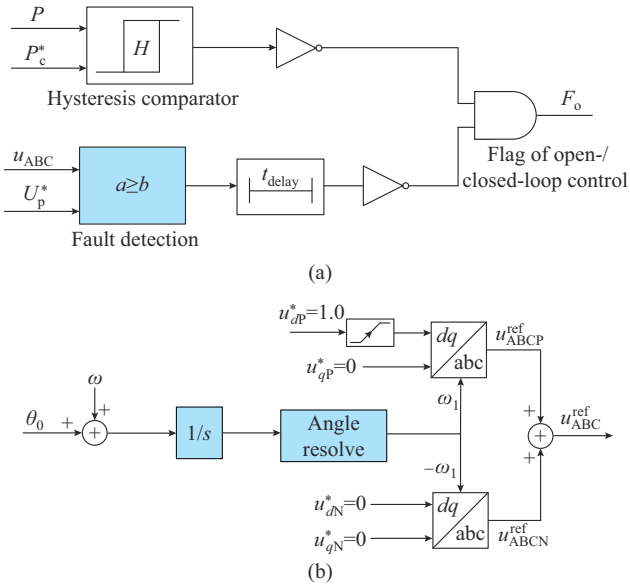

Fig. 16. Open-loop and closed-loop control of VSC-UHVDC. (a) Switching logic. (b) Open-loop control strategy.

There are two criteria for switching between open-loop and closed-loop control. ① The power comparison criterion: in order to prevent frequent switching of open loop and closed loop, the hysteresis comparator is used. The system switches from open-loop to closed-loop control when the active power exceeds P_c^*, and from closed-loop to open-loop control when it falls below $P_c^* - H$. ② The fault detection criterion: under low-power operation conditions, if any phase voltage drops, the system should switch from open-loop to closed-loop control to limit fault overcurrent.

To ensure a smooth transition between open-loop to closed-loop control and avoid voltage jumps during the switching process, a switching logic has been designed. ① The phase for dq-axis transformation remains unchanged: during open-loop control, the system automatically generates

the *dq*/abc axis transformation phase. When switching to closed-loop control, it is important to maintain the same phase generated by the system. ② During open-loop control, the PI controllers of outer AC voltage and inner current loop are locked. The modulation wave generated by closed-loop control at the moment of open-loop switching to closed-loop control is determined by voltage feedforward to ensure smooth switching of the modulation wave.

The same simulation conditions as those in Section VI are conducted. The VSC-UHVDC is started up with four 300 km no-load lines. During the black start operation, the VSC-UHVDC adopts the open-loop control strategy. The simulation results of open-loop and closed-loop adaptive control are shown in Fig. 17. The converter station can be successfully started without MHFR. After start-up, the system remains in no-load state and is switched to closed-loop control at 1.2 s. The high-frequency resonance gradually appears, further indicating that the risk of high-frequency resonance risk at the sending-end grid is relatively high when the closed-loop control strategy is adopted.

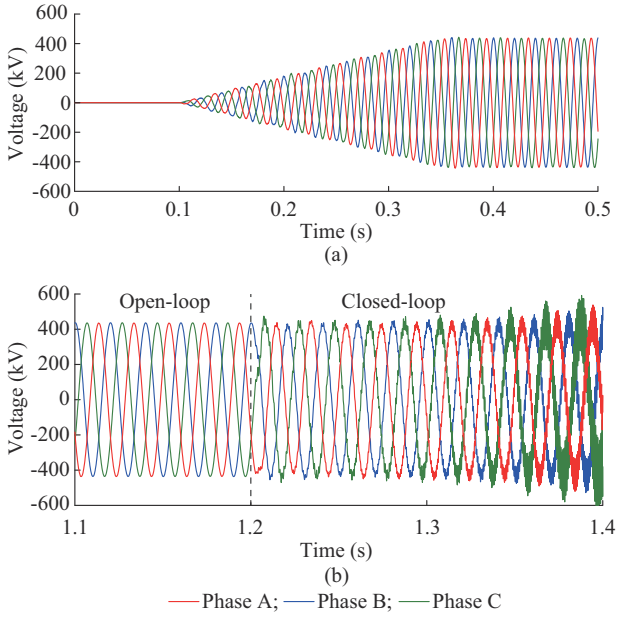

Fig. 17. Simulation results of adaptive open-loop and closed-loop control. (a) Black start process. (b) Switching to closed-loop control.

To verify the effectiveness of the smooth switching control logic, the dynamic characteristics of the system are compared before and after implementing the switching logic. The VSC-UHVDC switches from open-loop to closed-loop control when the active power of the converter exceeds 60 MW. As shown in Fig. 18, before adopting the smooth switching logic, there is a significant impact on the AC bus voltage during switching, with the maximum root mean square (RMS) voltage reaching 640 kV. With the implementation of the smooth switching logic, the impact on the system during the switching process is reduced, enabling smooth transitions between open-loop and closed-loop control.

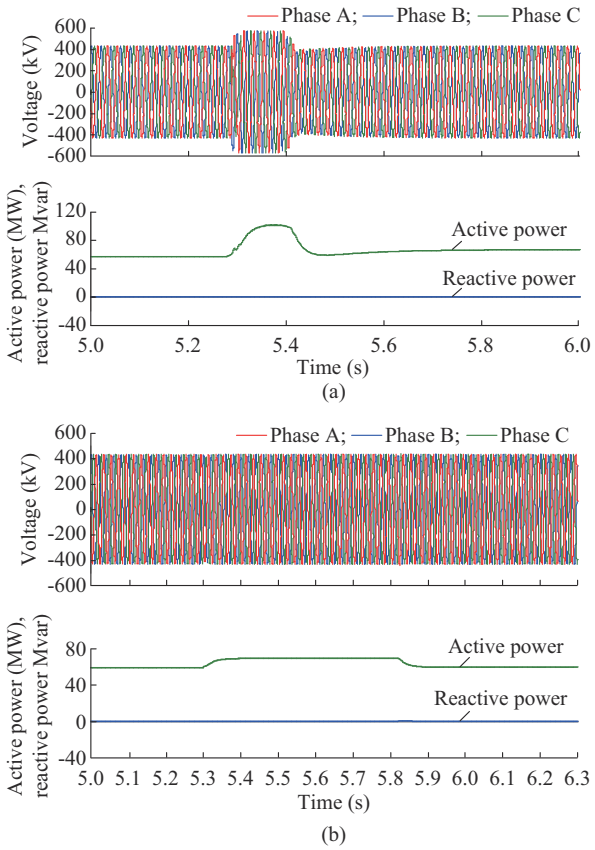

Fig. 18. Switching process of open-loop and closed-loop control before and after adopting a smooth switching logic. (a) Before adopting smooth switching logic. (b) After adopting smooth switching logic.

VIII. Conclusion

This paper explores the MHFR characteristics and suppression strategies in VSC-UHVDC for large-scale renewable energy transmission, and draws the following conclusions.

1) Both voltage single-loop control and voltage-current double-loop control for the VSC-UHVDC at the sending end pose a risk of MHFR. Considering the dynamic characteristics of the system comprehensively, it is not recommended to adopt the voltage single-loop control strategy.

2) The key factors affecting the impedance characteristics include the AC voltage control, voltage feedforward, inner current loop, PSNSIC, and control delay. The AC voltage control, which introduces new control delay characteristics and interacts with voltage feedforward, significantly impacts the impedance characteristics of converter.

3) Mid- and high-frequency impedance reshaping measures for VSC-UHVDC based on control system optimization are proposed, including voltage coordinated optimization control, reduction of proportional coefficient of the PI controller in inner current loop, optimization of *dq*-axis current decoupling control, and reduction of control delay.

4) The risk of MHFR is relatively high during black start operation under closed-loop control. Smooth open-loop and closed-loop adaptive control can be adopted. Open-loop control is adopted during black start operation to ensure that the system operates stably. The smooth switching logic is designed to achieve a seamless transition from open-loop to

closed-loop control.

APPENDIX A

The short-circuit current of the arm bridge is evaluated during a three-phase short-circuit fault in the AC grid with different impedance reshaping measure, including voltage coordinated optimization control, as well as adding low-pass filters both to voltage feedforward and outer AC voltage loop.

As depicted in Fig. A1, the maximum short-circuit current of the arm bridge is 1579 A when employing voltage coordinated optimization control, and 2492 A when adding low-pass filters, respectively, which demonstrates that the voltage coordinated optimization control exhibits better dynamic performance.

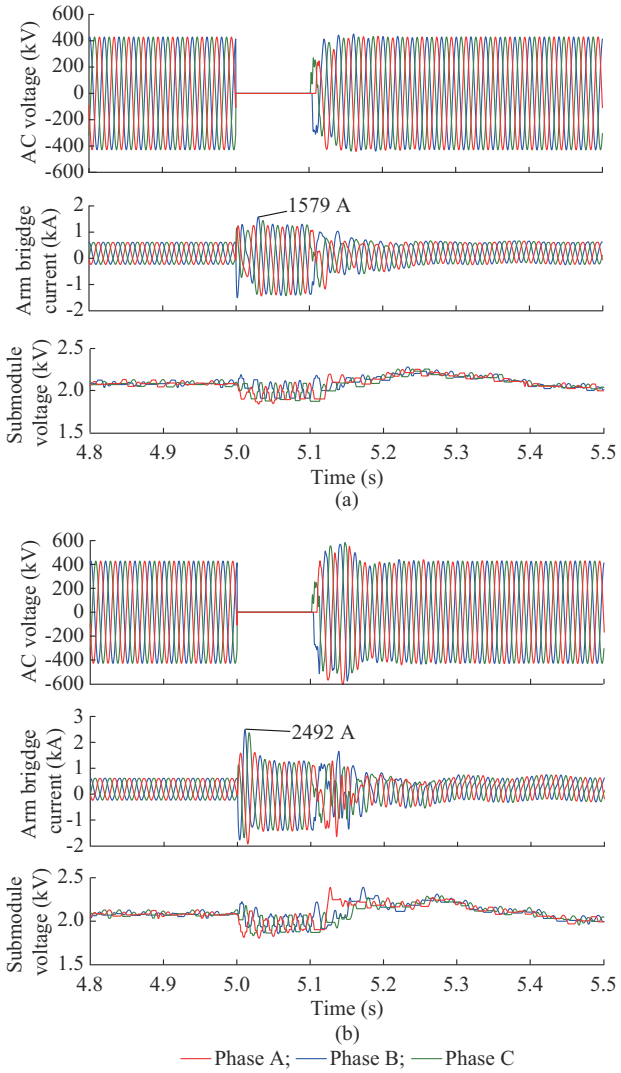

Fig. A1. Three-phase short-circuit fault response characteristics with different impedance reshaping measure. (a) Voltage coordinated optimization control. (b) Adding low-pass filters both to voltage feedforward and outer AC voltage loop.

REFERENCES

[1] B. Xin, M. Guo, S. Wang *et al*., "Friendly HVDC transmission technologies for large-scale renewable energy and their engineering practice," *Automation of Electric Power Systems*, vol. 45, no. 22, pp. 1-8, Nov. 2021.

[2] J. Wen, P. Meng, W. Xiang *et al*., "Unified high voltage direct current converter topology dedicated for new power systems," *New Type Power Systems*, vol. 1, no. 1, pp. 84-98, Jun. 2023.

[3] J. Xu, H. Jing, and C. Zhao, "Reliability modeling of MMCs considering correlations of the requisite and redundant submodules," *IEEE Transactions on Power Delivery*, vol. 33, no. 3, pp. 1213-1222, Oct. 2018.

[4] W. Wang, G. Li, and J. Guo, "Large-scale renewable energy transmission by HVDC: challenges and proposals," *Engineering*, vol. 19, no. 2022, pp. 252-267, Dec. 2022.

[5] M. Cheah-mane, L. Sainz, J. Liang *et al*., "Criterion for the electrical resonance stability of offshore wind power plants connected through HVDC links," *IEEE Transactions on Power Systems*, vol. 32, no. 6, pp. 4579-4589, Nov. 2017.

[6] H. Lin, H. S.-H. Chung, R. Shen *et al*., "Enhancing stability of DC cascaded systems with CPLs using MPC combined with NI and accounting for parameter uncertainties," *IEEE Transactions on Power Electronics*, vol. 39, no. 5, pp. 5225-5238, May 2024.

[7] B. Yuan, X. Li, C. Yin *et al*., "Mechanism and suppression strategy of high-frequency oscillation caused by integration of islanded renewable energy station into MMC-HVDC system," *Automation of Electric Power Systems*, vol. 47, no. 4, pp. 133-141, Feb. 2023.

[8] L. Gao, J. Lyv, and X. Cai, "Analysis of mid-frequency oscillation characteristics in Rudong MMC-HVDC system for offshore wind farms," *Power System Technology*, vol. 47, no. 9, pp. 3495-3506, Sept. 2023.

[9] J. Feng, C. Fu, C. Zou *et al*., "Impedance modeling and mid- and high-frequency resonance characteristic analysis for flexible DC converter with *V/f* control," *Automation of Electric Power Systems*, vol. 46, no. 4, pp. 143-152, Feb. 2022

[10] N. Mei, B. Yuan, T. Li *et al*., "Study on control strategy of bipolar VSC station connected to islanded renewable power plant," *Power System Technology*, vol. 42, no. 11, pp. 3575-3582, Nov. 2018.

[11] X. Cai, W. Huang, G. Li *et al*., "Research on operation control strategy of large-scale photovoltaic cluster transmission via grid-forming VSC-HVDC," *Proceedings of the CSEE*, vol. 43, no. 22, pp. 8734-8744, Nov. 2023.

[12] H. Lin, T. Xue, J. Lyu *et al*., "Impact of different AC voltage control modes of wind-farm-side MMC on stability of MMC-HVDC with offshore wind farms," *Journal of Modern Power Systems and Clean Energy*, vol. 11, no. 5, pp. 1687-1699, Sept. 2023.

[13] D. Zhang, X. Chen, S. Yang *et al.*, "Analysis of high-frequency resonance and suppression strategy of photovoltaic power plant with static reactive power compensation device," *Proceedings of the CSEE*, vol. 43, no. 24, pp. 9580-9593, Dec. 2023.

[14] C. Zou, H. Rao, S. Xu *et al*., "Analysis of resonance between a VSC-HVDC converter and the AC grid," *IEEE Transactions on Power Electronics*, vol. 33, no. 12, pp. 10157-10168, Dec. 2018.

[15] X. Guo, B. Liu, H. Mei *et al*., "Analysis and suppression of resonance between AC and DC systems in Chongqing-Hubei back-to-back HVDC project of China," *Automation of Electric Power Systems*, vol. 44, no. 20, pp. 157-164, Oct. 2020.

[16] J. Feng, C. Zou, S. Yang *et al*., "Accurate impedance modeling and characteristic analysis of VSC-HVDC system for mid- and high-frequency resonance problems," *Proceedings of the CSEE*, vol. 40, no. 15, pp. 4805-4819, Aug. 2020.

[17] J. Lyu, X. Zhang, X. Cai *et al*., "Harmonic state-space based small-signal impedance modeling of a modular multilevel converter with consideration of internal harmonic dynamics," *IEEE Transactions on Power Electronics*, vol. 34, no. 3, pp. 2134-2148, Mar. 2019.

[18] J. Man, X. Xie, S. Xu *et al*., "Frequency-coupling impedance model based analysis of a high-frequency resonance incident in an actual MMC-HVDC system," *IEEE Transactions on Power Delivery*, vol. 35, no. 6, pp. 2963-2971, Dec. 2020.

[19] M. Cespedes and J. Sun, "Impedance modeling and analysis of grid-connected voltage source converters," *IEEE Transactions on Power Electronics*, vol. 29, no. 3, pp. 1254-1261, Mar. 2014

[20] K. Ji, G. Tang, H. Pang *et al*., "Impedance modeling and analysis of MMC-HVDC for offshore wind farm integration," *IEEE Transactions of Power Delivery*, vol. 35, no. 3, pp. 1488-1501, Jun. 2020.

[21] J. Zhu, J. Hu, L. Lin *et al*., "High-frequency oscillation mechanism analysis and mitigation method of VSC-HVDC," *IEEE Transactions on Power Electronics*, vol. 35, no. 9, pp. 8892-8896, Sept. 2020.

[22] Y. Rao, J. Lyu, Y. Wang *et al.*, "Adaptive mitigation control for wideband oscillations of offshore wind farms with MMC-HVDC system,"

CSEE Journal of Power and Energy Systems, doi: 10.17775/CSEEJPES.2021.06530

[23] B. Pang, H. Nian, and Y. Xu, "Mechanism analysis and damping method for high frequency resonance between VSC-HVDC and the wind farm," *IEEE Transactions on Energy Conversion*, vol. 36, no. 2, pp. 984-994, Jun. 2021.

[24] J. Wang, W. Chen, Y. Liu *et al*., "High frequency resonance analysis and impedance reshaping control of MMC-HVDC system based on frequency coupling impedance model," *Journal of Modern Power Systems and Clean Energy*, vol. 12, no. 2, pp. 646-657, Mar. 2024.

[25] Y. Hou, C. Liu, Y. Wang *et al.*, "Research on the suppression strategy of high-frequency resonance for MMC-HVDC," *Proceedings of the CSEE*, vol. 41, no. 11, pp. 3741-3750, Jun. 2021.

[26] K. Ji, H. Pang, Z. He *et al.*, "Active/passive method-based hybrid high-frequency damping design for MMCs," *IEEE Journal of Emerging and Selected Topics in Power Electronics*, vol. 9, no. 5, pp. 6086-6098, Oct. 2020.

Junjie Feng received the B.Eng. and M.Eng. degrees in electrical engineering from South China University of Technology, Guangzhou, China, in 2016 and 2019, respectively. He is currently pursuing the Ph.D. degree at Huazhong University of Science and Technology, Wuhan, China. He is also an Engineer with Electric Power Research Institute, China Southern Power Grid, Guangzhou, China. His research interests include renewable energy integration and voltage source converter-based high voltage direct current (VSC-HVDC).

Wang Xiang received the B.Eng. and Ph.D. degrees in electrical engineering from Huazhong University of Science and Technology, Wuhan, China, in 2012 and 2017, respectively. He was a visiting Ph.D. student at the University of Aberdeen, Aberdeen, UK, and the University of Strathclyde, Glasgow, UK, in 2014 and 2016, respectively. He was with the University of Strathclyde from 2018 to 2021. Currently, he is a Professor at School of Electrical and Electronics Engineering, Huazhong University of Science and Technology. His main research interests include modular multilevel converter-based high voltage direct current (MMC-HVDC), high power DC/DC converters, DC grid, and offshore wind power integration.

Jinyu Wen received the B.Eng. and Ph.D. degrees both in electrical engineering from Huazhong University of Science and Technology (HUST), Wuhan, China, in 1992 and 1998, respectively. He was a Visiting Student from 1996 to 1997 and Research Fellow from 2002 to 2003 both at the University of Liverpool, Liverpool, UK, and a Senior Visiting Researcher at the University of Texas at Arlington, Arlington, USA, in 2010. From 1998 to 2002, he was the Director Engineer in XJ Electric Co. Ltd., Xuchang, China. In 2003, he joined the HUST and now is a Professor with the School of Electrical and Electronics Engineering, HUST. His current research interests include renewable energy integration, energy storage application, DC grid, and power system operation and control.

Chuang Fu received the B.S. degree from the Sichuan Institute of Technology, Chengdu, China, in 1996, and the M.S. and Ph.D. degrees from Huazhong University of Science and Technology, Wuhan, China, in 1999 and 2003, respectively. He is currently working at the Electric Power Research Institute, China Southern Power Grid, Guangzhou, China. His research interests include flexible alternative current transmission system (FACTS), power system analysis, voltage stability, and operation of power systems.

Qingming Xin received the B.Eng. degree from Zhejiang University, Hangzhou, China, in 2009, and the Ph.D. degree from Huazhong University of Science and Technology, Wuhan, China, in 2014. He is currently working at the Electric Power Research Institute, China Southern Power Grid, Guangzhou, China. His research interest includes high voltage direct current and renewable energy integration.

Xiaobin Zhao received the B.S. degree from Huazhong University of Science and Technology, Wuhan, China, in 2008, and the M.Eng. degree from Tsinghua University, Beijing, China, in 2021. He is currently working at the Electric Power Research Institute, China Southern Power Grid, Guangzhou, China. His research interest includes high voltage direct current and renewable energy integration.

Changyue Zou received the B.S. and Ph.D. degrees from Huazhong University of Science and Technology, Wuhan, China, in 2010 and 2015, respectively. He is currently an Electrical Engineer with the Electric Power Research Institute, China Southern Power Grid, Guangdong, China. His main research interests include control and design of VSC-HVDC.

Biyue Huang received the B.S. and Ph.D. degrees from Huazhong University of Science and Technology, Wuhan, China, in 2016 and 2021, respectively. She is currently working at the Electric Power Research Institute, China Southern Power Grid, Guangdong, China. Her main research interests include renewable energy integration and VSC-HVDC.

Zhiyong Yuan received the B. Eng. degree from Chongqing University, Chongqing, China, in 2001, and the Ph.D. degree from Tsinghua University, Beijing, China, in 2007. He is currently working at the Electric Power Research Institute, China Southern Power Grid, Guangzhou, China. His research interest is high voltage direct current transmission.